Phys. Status Solidi RRL **11**, No. 2, 1600395 (2017) / **DOI** 10.1002/pssr.201600395

pss +++rapid research letters+++
www.pss-rapid.com

Hole-extraction layer dependence of defect formation and operation of planar $CH_3NH_3PbI_3$ perovskite solar cells

Duc Cuong Nguyen[1], Sung-yoon Joe[1], Na Young Ha[1,2], Hui Joon Park[1,3], Ji-Yong Park[1,2], Y. H. Ahn[1,2], and Soonil Lee[*,1,2]

[1] Department of Energy Systems Research, Ajou University, Suwon 16499, Korea
[2] Department of Physics, Ajou University, Suwon 16499, Korea
[3] Department of Electrical and Computer Engineering, Ajou University, Suwon 16499, Korea

Received 20 November 2016, revised 12 December 2016, accepted 16 December 2016
Published online 23 December 2016

Keywords $CH_3NH_3PbI_3$, solar cells, interface defects, bulk defects, charge carrier recombination, capacitance

[*] Corresponding author: e-mail soonil@ajou.ac.kr, Phone: +82-31-219-2582, Fax: +82-31-219-1748

Three planar $CH_3NH_3PbI_3$ ($MAPbI_3$) solar cells having the same structure except a hole-extraction layer (HEL) showed distinctive difference in operation characteristics. Analysis of frequency-dependent capacitance and dielectric-loss spectra of the three $MAPbI_3$ devices showed two types of recombination-loss channels with different time constants that we attributed respectively to interface and bulk defects. Discrepancy in defect formation among the three devices with a HEL of PEDOT:PSS, NiO_x, or Cu-doped NiO_x was not surprising because grain-size distribution and crystalline quality of $MAPbI_3$ can be affected by surface energy and morphology of underlying HELs. We were able to quantify interface and bulk defects in these $MAPbI_3$ solar cells based on systematic and simultaneous simulations of capacitance and dielectric-loss spectra, and current–voltage characteristics by using the device simulator SCAPS.

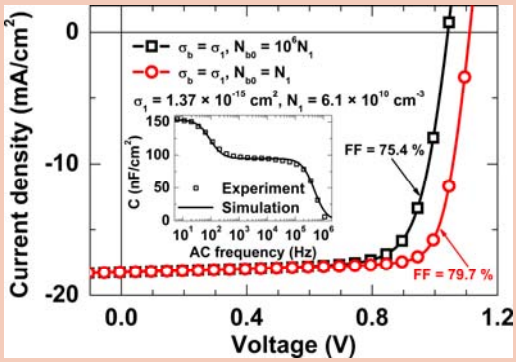

Defect density reduction is essential for efficient planar solar cells. Defect density in $MAPbI_3$ layers, with respect to which an open-cell voltage and a fill factor vary, can be investigated by using capacitance–frequency spectra.

1 Introduction Studies of organolead trihalide perovskite (OTP) solar cells progressed rapidly in recent years. For example, power conversion efficiency (PCE) improved from modest 3.81% to impressive 20.2% in six years [1, 2]. In addition to device architecture modification, utilization of various organic and inorganic materials to improve charge carrier extraction and/or to minimize their recombination emerged as interesting research topics. Passivation of electron traps in OTP layers by 1-(3-methoxy-carbonyl)-propyl-1-phenyl-(6,6)C61 (PCBM) was one of successful results of such studies [3]. In a typical planar heterojunction structure, a PCBM electron-extraction layer (EEL) is deposited onto an OTP active layer (AL), which allows passivation of surface- and bulk-defects of OTP layers by PCBM. Nevertheless, formation and/or growth of OTP domains are not affected by posterior PCBM coating. On the contrary, hole-extraction layers (HELs) such as sol–gel NiO_x onto which ALs are deposited may affect the formation and growth of polycrystalline OTP and can result in different types and amounts of defects in OTP layers.

In this work, we fabricated three types of planar solar cells (PSCs) by using identical $CH_3NH_3PbI_3$ ($MAPbI_3$) AL and PCBM EEL combination with three different HELs. Interestingly, the three $MAPbI_3$ PSCs showed noticeably

different current density–voltage (J–V) curves and large PCE discrepancies. Preliminary analysis by using SCAPS, a device simulator developed by Burgelman's group at the University of Gent [4], showed that variation in J–V curves, in spite of similar photon harvesting by $MAPbI_3$ layers, can be attributed to discrepancy in charge recombination at defects. According to aforementioned PCBM passivation effects, defect-induced recombination at $MAPbI_3$-PCBM interface is not likely to be responsible for the observed discrepancy in J–V curves. However, interfacial defects at HEL-AL junctions can be responsible for sizable hole-recombination. Moreover, HELs, onto which $MAPbI_3$ ALs are spin-coated, can produce different $MAPbI_3$ bulk-defect characteristics (density and hole-capture cross-section) as grain size distribution and crystalline quality of $MAPbI_3$ can be greatly affected by surface energy and morphology of underlying HELs [5].

Impedance spectroscopy (IS) was used for quantitative investigation of defect effects in planar $MAPbI_3$ solar cells. Capacitance–conductance–frequency (C–G–f) spectra were measured, and, in particular, C–f and G/ω–f (G/ω represents dielectric loss) spectra were fitted to an equivalent circuit (EC) model to separate contributions of different defects. Moreover, we simulated C–f and G/ω–f curves by using the SCAPS based on an actual device architecture and specific defect distributions. Such frequency domain simulations were useful in identifying defect types and defect densities. Because additional steady-state simulations with the same microscopic models produced J–V curves, we were able to elucidate microscopic origin of operation parameter values that limit PCEs of planar $MAPbI_3$ solar cells.

2 Experimental section Planar $MAPbI_3$ solar cells with a structure of FTO/HEL/$MAPbI_3$/PCBM/LiF/Al were fabricated on 7.33 Ω sq^{-1} FTO-coated glass substrates by using a HEL of PEDOT:PSS, un-doped NiO_x, or Cu-doped NiO_x. $MAPbI_3$ PSCs are designated as PEDPSS, $unNiO_x$, and $CuNiO_x$ according to their HELs. 50 nm thick PCBM and LiF/Al were an EEL and a cathode, respectively. FTO anodes were patterned by using zinc powder and hydrochloric acid, thoroughly cleaned, and treated with UV-ozone for 30 min right before HEL deposition. PEDOT:PSS (CLEVIOS P VP AI 4083) was filtered through a 0.45 μm PVDF filter before casting on patterned FTO-coated glass substrates. Spin-coating at 3,000 rpm for 60 s and annealing at 150 °C for 20 min in air produced a 40 nm thick PEDOT:PSS layer. NiO_x precursor was an equimolar mixture of nickel acetate tetrahydrate and ethanolamine in 2-methoxyethanol. The mixture was stirred at room temperature for 12 h and then stored in fridge for later use. Copper acetate monohydrate was added to this stock solution to make a precursor for Cu-doped NiO_x. Cu to Ni molar ratio was 10%. Both un-doped and Cu-doped NiO_x HELs were deposited by spin-coating respective precursors at 4,000 rpm for 30 s, and then annealing at 550 °C for 30 min in air. Thickness of both NiO_x HELs was determined to be ~7 nm from spectroscopic ellipsometry measurements. $MAPbI_3$ active layers were made by combining single-step coating and toluene dripping methods [6]. After baking at 100 °C for 10 min in N_2-filled glove box, ~210 nm $MAPbI_3$ layers were formed; see Fig. S1 in Supporting Information (SI).

3 Results and discussion J–V curves of the three PSCs measured under AM 1.5G illumination conditions are shown in Fig. 1. To be free from hysteresis effects, J–V curves were measured using the same voltage sweep conditions (Fig. S2). Performance parameters of the device PEDPSS are open-circuit voltage (V_{OC}) of 0.816 V, short-circuit current (J_{SC}) of 15.8 mA/cm^2, fill factor (FF) of 70.4%, and PCE of 9.07%. The device $unNiO_x$ shows higher PCE of 10.3% with improved V_{OC} of 0.927 V and J_{SC} of 17.9 mA/cm^2, but lower FF of 62.1%. The device $CuNiO_x$ shows the best performance with V_{OC} of 1.04 V, J_{SC} of 18.1 mA/cm^2, and FF of 75.5% to result in PCE of 14.2%. Consistently, fitting of the J–V curves to Shockley diode equation with parasitic resistances show the lowest series and the highest shunt resistances; see Table S1 in SI.

Low optical transmittance of PEDOT:PSS compared to those of un-doped and Cu-doped NiO_x is the main reason for low J_{SC} of the PEDPSS (Fig. S3). Additionally, large mismatch between work function (WF) of PEDOT:PSS (4.8 eV) and valence band (VB) of $MAPbI_3$ (5.43 eV) is responsible for low V_{OC} of this device [7]. However, WF of un-doped NiO_x is larger than that of PEDOT:PSS so that VB-WF mismatch is reduced to result in modest V_{OC} improvement for the device $unNiO_x$. It seems that the lowest FF of the $unNiO_x$ is mainly due to excessive dark saturation current, J_0 of 3.195×10^{-4} mA/cm^2, and high ideality factor, n of 3.30, in the parasitic-resistance diode model.

Noticeably larger V_{OC} and FF of the device $CuNiO_x$ can be attributed to more favorable VB-WF energy alignment and better hole extraction from $MAPbI_3$ without significant recombination loss. Markedly larger photo-shunt

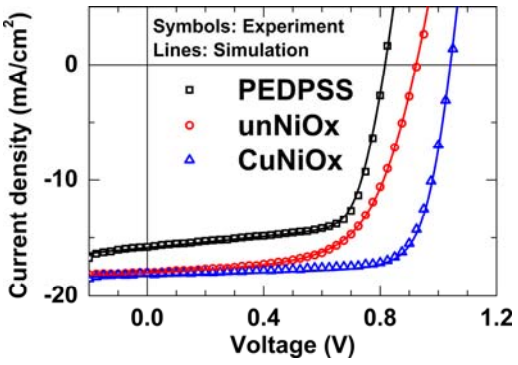

Figure 1 Experimental (symbols) and simulated (solid lines) J–V curves for three planar $MAPbI_3$ solar cells with a different HEL: PEDPSS, $unNiO_x$, and $CuNiO_x$. J–V curves were measured under AM 1.5G illumination condition, and J–V simulations were done by using the device simulator SCAPS.

resistance is a corroborating evidence for reduced recombination loss. Because $MAPbI_3$ solar cells are known to be susceptible to carrier loss due to recombination at defects [3, 8–9], it is reasonable to argue that there were less defects in a $MAPbI_3$ AL of the $CuNiO_x$ compared to those of the other two devices.

C–f and *G/ω–f* spectra in Fig. 2 manifest different defect distribution among the three $MAPbI_3$ PSCs. These spectra were measured at 0 V in dark. We note that the *C–f* spectra show two-step features with distinct time constants. Inset shows an equivalent circuit to which we fitted *C–f* and *G/ω–f* spectra simultaneously. In IS, time constants are commonly modeled by resistance–capacitance (*R–C*) pairs. We incorporated two *R–C* pairs to quantify time constants corresponding to respective recombination processes within $MAPbI_3$ ALs (R_b and C_b) and at interfaces between ALs and HELs (R_i and C_i). On the other hand, R_{tr} represents charge carrier transport within $MAPbI_3$ ALs and/or across AL-HEL interfaces. R_s is a series resistance, and CPE_g is a constant phase element that we used for better fitting in the frequency range from 5×10^2 to 1×10^5 Hz, instead of ideal geometrical capacitance C_g for stacked layers. Nonideal capacitive behavior may come from non-Debye response of $MAPbI_3$ material [10].

Solid lines in Fig. 2 show good agreement between fitting results and measured *C–f* and *G/ω–f* spectra. Values of EC parameters are summarized in Table S2. As listed in Table 1, respective recombination time constants due to bulk defects ($\tau_b = R_bC_b$) are 102 ms, 8.08 ms and 112 ms for the device PEDPSS, $unNiO_x$, and $CuNiO_x$. Time constants for interface-defect recombination ($\tau_i = R_iC_i$) are 20.9 ms, 1.11 ms and 24.2 ms for the PEDPSS, $unNiO_x$, and $CuNiO_x$ device, respectively. We note that τ_i is about 5–7 times smaller than τ_b, and that both time constants of the device $unNiO_x$ are particularly small. In short, small recombination time constants are detrimental to device operation, and further passivation, in particular at HEL interfaces, are important.

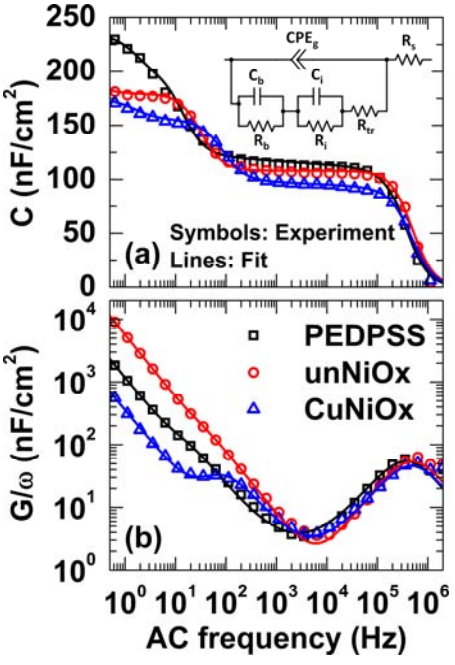

Figure 2 Experimental (symbols) and best-fit (solid lines) *C–f* (a) and *G/ω–f* (b) spectra for the $MAPbI_3$ solar cells having different HELs. Inset shows an equivalent circuit to which *C–f* and *G/ω–f* curves were fitted.

Table 1 Performance parameters and charge recombination time constants due to bulk and interface defects for the three $MAPbI_3$ planar solar cells. Time constants were estimated from resistance and capacitance values extracted by fitting *C–f* and *G/ω–f* spectra according to an equivalent circuit model in Fig. 2. Numbers in parentheses correspond to SCAPS simulation results.

sample ID	PEDPSS	$unNiO_x$	$CuNiO_x$
V_{OC} (V)	0.816 (0.817)	0.927 (0.924)	1.04 (1.04)
J_{SC} (mA/cm^2)	15.8 (15.9)	17.9 (18.0)	18.1 (18.2)
FF (%)	70.4 (69.3)	62.1 (61.8)	75.5 (75.4)
PCE (%)	9.07 (8.97)	10.3 (10.3)	14.2 (14.3)
τ_b (ms)	102	8.08	112
τ_i (ms)	20.9	1.11	24.2

Next, we discuss defect effects further based on the device simulator SCAPS (ver. 3.3.03) that is basically a drift-diffusion equation solver [4]. For SCAPS simulations, we have to specify details of device structure and material properties. Important parameter values for simulations are specified in SI (see Simulation Model) and listed in Table S3. Preliminary SCAPS simulations indicated that proper defect models were essential in accounting for variations in *J–V* curves and impedance spectra simultaneously. Specifically, we found that defects at HEL-$MAPbI_3$ interfaces had to be a neutral type with Gaussian energetic distribution ((Eq. S1) in SI). On the other hand, it seemed that bulk defects that were uniformly distributed throughout $MAPbI_3$ ALs consisted of both acceptor- and donor-type defects with separate Gaussian energetic distributions. Numerous simulations with various previously reported defects [11] showed that negatively-charged methylammonium (V'_{MA}) and positively-charged iodine ($V_I^{\bullet}$) vacancies were most likely candidates for bulk defects to account for *J–V* curves and impedance spectra simultaneously. Parameter values for V'_{MA} and $V_I^{\bullet}$ distributions are listed in Table S4.

SCAPS simulations based on the microscopic model of neutral interface defects and charged-vacancy bulk defects showed distinctive changes in *C–f*, *G/ω–f*, and *J–V* curves in response to variations of carrier capture cross-section and total defect density. In particular, it was interesting to note that bulk defect variation resulted in substantial changes to *J–V* curves, but not to *C–f* spectra. On the contrary, effects of interface defect variations were prominent in *C–f* spectra, but not in *J–V* curves. For example, four orders of magnitude increase of total bulk defect concentration N_{b0} resulted in only a slight increase of the second

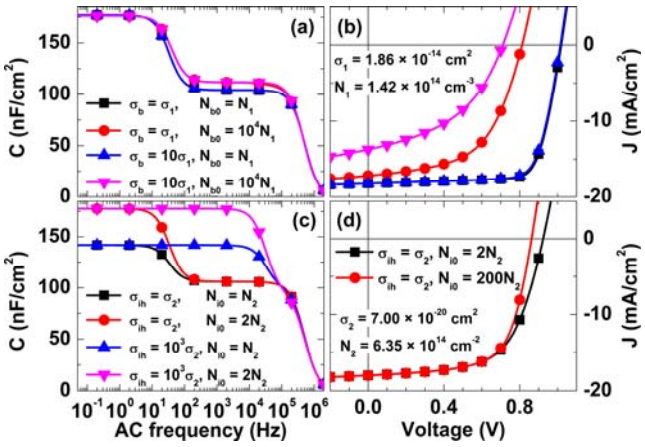

Figure 3 Typical SCAPS simulation results showing changes in *C–f* and *J–V* curves with respect to capture cross-sections and total defect concentrations of bulk (σ_b and N_{b0}) and interface (σ_{ih} and N_{i0}) defects in $MAPbI_3$ planar solar cells: (a) *C–f* and (b) *J–V* curve variations with respect to σ_b and N_{b0}, and (c) *C–f* and (d) *J–V* curve changes with respect to σ_{ih} and N_{i0}. Simulations were done with the general parameter values for the $unNiO_x$ and the parameter values for energetic distributions of bulk and interface defects in Table S3.

capacitance plateau in a medium frequency range (from 104.2 nF/cm^2 to 111.8 nF/cm^2 at 1000 Hz) as shown in Fig. 3(a). Similarly, 1 order of magnitude increase of capture cross-section of bulk defects σ_b barely produced any change in *C–f* spectra. However, same σ_b and N_{b0} increases resulted in substantial changes in *J–V* curves as Fig. 3(b) shows. In the case of interface defects, 1 order of magnitude larger total defect concentration N_{i0} produced noticeable increase of the first capacitance plateau in a low frequency range (from 141.7 nF/cm^2 to 177.6 nF/cm^2 at 1 Hz) as seen in Fig. 3(c). Moreover, larger hole-capture cross-section σ_{ih} yielded not only increase of the second capacitance plateau, but also higher transition frequency (equivalent to smaller time constant) for the first capacitance plateau. On the other hand, only V_{OC} decreased noticeably, from 0.924 V to 0.863 V, in response to 2 orders of magnitude increase of N_{i0} as shown in Fig. 3(d).

Relying on distinctive contributions of interface and bulk defects to variations in *C–f*, *G/ω–f*, and *J–V* curves, we were able to quantify characteristics of both defects in the three $MAPbI_3$ PSCs. To begin with, we specified interface defect parameters σ_{ih} and N_{i0} by simulating *C–f* spectra. For example, it was found that characteristics frequency of 90 Hz and capacitance plateau of 152 nF/cm^2 of the $CuNiO_x$ were consistent with σ_{ih} of 8.50×10^{-15} cm^2 and N_{i0} of 2.65×10^{13} cm^{-2}. We note that characteristics frequency was determined not only by σ_{ih}, but also by hole-injection barrier $\Delta\varphi$ at HEL-$MAPbI_3$ junctions. Contributions of $\Delta\varphi$ were apparent in *G/ω–f* spectra, too (Fig. S4). Based on simultaneous agreement of *C–f* and *G/ω–f* spectra, we estimated $\Delta\varphi$ to be 0.03 eV for the device $CuNiO_x$. Following the same steps, we obtained σ_{ih} of 1.00×10^{-23} cm^2, N_{i0} of 5.50×10^{14} cm^{-2}, and $\Delta\varphi$ of 0.63 eV for the device PEDPSS. In the case of the device $unNiO_x$, parameters were estimated to be σ_{ih} of 7.00×10^{-20} cm^2, N_{i0} of 1.27×10^{15} cm^{-2}, and $\Delta\varphi$ of 0.23 eV. In short, the device $CuNiO_x$ had the smallest N_{i0}, but the largest σ_{ih}. Arguably, the smallest N_{i0} can be attributed to the large grain size of Cu-doped NiO_x, and the largest σ_{ih} to Cu precipitation at the surface [12–13]. On the contrary, the $unNiO_x$ device had the largest N_{i0} and modest σ_{ih} because of small NiO_x grain size and no metal impurity precipitation at the surface. The device PEDPSS showed intermediate N_{i0} and the smallest σ_{ih}, which was consistent with the growth of neat $MAPbI_3$ layers onto smooth PEDOT:PSS surfaces.

The aforementioned parameter values for σ_{ih}, N_{i0}, and $\Delta\varphi$ of the three $MAPbI_3$ PSCs were then used to estimate capture cross-section σ_b and total density N_{b0} of bulk defects by simulating *J–V* curves. The *J–V* simulation results (solid lines in Fig. 1) that show very good agreement with experimental data correspond to σ_b of 1.37×10^{-15}, 1.86×10^{-14}, and 2.00×10^{-16} cm^2, and N_{b0} of 6.10×10^{16}, 1.24×10^{17}, and 1.00×10^{17} cm^{-3} for the devices $CuNiO_x$, $unNiO_x$, and PEDPSS, respectively. The highest σ_b and N_{b0} of the device $unNiO_x$ indicate that this device suffered significant recombination loss due to bulk defects within $MAPbI_3$ ALs. The large recombination loss is consistent with the short τ_b obtained from the EC analysis of *C–f* and *G/ω–f* spectra. Oppositely, the device $CuNiO_x$ with smaller σ_b and N_{b0} was less susceptible to recombination loss at bulk defects compared to the device $unNiO_x$. Very good agreement between measured and simulated *J–V* curves automatically resulted in almost the same device performance parameters as listed in Table 1.

4 Conclusions We reported that the use of Cu-doped NiO_x as a HEL in $MAPbI_3$ PSCs resulted in substantial PCE improvement compared to similar PSCs with a HEL of either NiO_x or PEDOT:PSS. EC-based analysis of *C–f* and *G/ω–f* spectra showed two *RC* time-constant features that indicated occurrence of two different kinds of recombination losses. Similar to previous reports, we attributed these two losses to defect-induced recombination events. However, our two-defect model was different from the previous one that considered interface defects at $MAPbI_3$-EEL junctions together with bulk defects within a $MAPbI_3$ AL [3]. In our model, interface defects at HEL-$MAPbI_3$ junctions were considered, but those at $MAPbI_3$-EEL junctions were neglected due to PCBM passivation. Naturally, both bulk and interface defects were connected with grain-size distribution and crystalline quality in $MAPbI_3$ ALs, which were, in turn, affected by surface energy and morphology of underlying HELs. *C–f*, *G/ω–f*, and *J–V* data were analyzed further by using the device simulator SCAPS to quantify defect parameters and their respective effects on *C–f*, *G/ω–f*, and *J–V* curve shapes. Different response of *C–f*, *G/ω–f*, and *J–V* characteristics to variations in microscopic defect models was the basis of our quantifi-

cation of defect parameters. The systematic approach we reported in this work is general enough to be applied to other solar cell systems to identify and quantify defects hampering device operation. Detailed identification and quantification of defects are prerequisites for developing efficient passivation technique that can minimize detrimental defect effects to improve device performance further.

Supporting Information Additional supporting information may be found in the online version of this article at the publisher's website. There, device characterization methods, *J–V* fitting parameter values based on a diode model with parasitic resistances, equivalent circuit parameters extracted from *C–f* and *G*/*ω*–*f* curve fittings, models and parameter values for SCAPS simulations, top-view SEM images and corresponding grain-size distributions of $MAPbI_3$ layers deposited onto different HELs, voltage-scan direction dependence of *J–V* curve variations, EQE and integrated photocurrent spectra of the three $MAPbI_3$ planar solar cells, and *C–f* and *G*/*ω*–*f* spectra with respect to hole-injection barrier are given.

Acknowledgements This research was supported by the National Research Foundation of Korea (NRF) Grant (No. NRF-535 2014R1A2A2A01005632) which is funded by the Korea government (MEST).

References

[1] A. Kojima, K. Teshima, Y. Shirai, and T. Miyasaka, J. Am. Chem. Soc. **131**, 6050–6051 (2009).
[2] W. S. Yang, J. H. Noh, N. J. Jeon, Y. C. Kim, S. Ryu, J. Seo, and S. I. Seok, Science **348**(6240), 1234–1237 (2015).
[3] Y. Shao, Z. Xiao, C. Bi, Y. Yuan, and J. Huang, Nature Commun. **5**, 5784 (2014).
[4] M. Burgelman, P. Nollet, and S. Degrave, Thin Solid Films **361**, 527–532 (2000).
[5] C. Bi, Q. Wang, Y. Shao, Y. Yuan, Z. Xiao, and J. Huang, Nature Commun. **6**, 7747 (2015).
[6] N. J. Jeon, J. H. Noh, Y. C. Kim, W. S. Yang, S. Ryu, and S. I. Seok, Nature Mater. **13**, 897–903 (2014).
[7] H. S. Jung and N.-G. Park, Small **11**(1), 10–25 (2015).
[8] M. L. Agiorgousis, Y-Y. Sun, H. Zeng, and S. Zhang, J. Am. Chem. Soc. **136**(41), 14570–14575 (2014).
[9] L. K. Ono and Y. Qi, J. Phys. Chem. Lett. **7**(22), 4764–4794 (2016).
[10] J. Bisquert, L. Bertoluzzi, I. Mora-Sero, and G. Garcia-Belmonte, J. Phys. Chem. C **118**, 18983−18991 (2014).
[11] W.-J. Yin, T. Shi, and Y. Yan, Appl. Phys. Lett. **104**, 063903 (2014).
[12] K. H. Kim, C. Takahashi, Y. Abe, and M. Kawamura, Optik **125**, 2899–2901 (2014).
[13] S. C. Chen, T. Y. Kuo, Y. C. Lin, and H. C. Lin, Thin Solid Films **519**, 4944–4947 (2011).